catalysts

MDPI

Article

Spinel $LiMn_2O_4$ as Electrocatalyst toward Solid-State Zinc–Air Batteries

Guoqing Zhang [1,*], Peng Zhang [2], Shuying Kong [1] and Binbin Jin [1]

[1] Chongqing Key Laboratory of Inorganic Special Functional Materials, Yangtze Normal University, 16 Juxian Road, Fuling , Chongqing 408100 , China
[2] College of Materials Science and Engineering, Yangtze Normal University, 16 Juxian Road, Fuling, Chongqing 408100, China
* Correspondence: yzhanggq@163.com or zhangguoqing@yznu.edu.cn

Abstract: Efficient oxygen reduction reaction (ORR) electrocatalysts are the key to advancement of solid-state alkaline zinc–air batteries (ZAB). We demonstrate an electrocatalyst, spinel lithium-manganese oxide $LiMn_2O_4$ (LMO) by a simple hydrothermal method. Scanning electron microscope (SEM), X-ray diffraction (XRD), and Raman spectra indicate that the as-synthesized $LiMn_2O_4$ presents nanoscale irregular-shaped particles with the well-known spinel structure. The polarization curve, chronoamperometery curve, and linear scanning voltammograms of rotating disk electrode (RDE) results reveal that the as-synthesized $LiMn_2O_4$ possesses a higher electrocatalytic activity than that of electrolytic manganese dioxide for the ORR. A solid-state zinc–air cell with $LiMn_2O_4$ as the air electrode catalyst has a long voltage plateau of discharge and a discharge capacity of 188.4 mAh at a constant discharge current density of 10 $mA{\cdot}cm^{-2}$. In summary, spinel $LiMn_2O_4$ in which the JT effect enables electron hoping between Mn^{3+} and Mn^{4+} can be regarded as an effective robust oxygen reduction catalyst.

Keywords: electrocatalyst; oxygen reduction reaction; air electrode; electrocatalytic activity; solid-state zinc–air cell

Citation: Zhang, G.; Zhang, P.; Kong, S.; Jin, B. Spinel $LiMn_2O_4$ as Electrocatalyst toward Solid-State Zinc–Air Batteries. *Catalysts* **2023**, *13*, 860. https://doi.org/10.3390/catal13050860

Academic Editors: Liangliang Feng and Yipu Liu

Received: 30 March 2023
Revised: 2 May 2023
Accepted: 4 May 2023
Published: 9 May 2023

1. Introduction

Alkaline solid-state zinc–air batteries (ZAB) assembled with a gel polymer electrolyte have been widely used in flexible electronic devices in recent years due to their portability, wearability, safety and high specific energy (theoretical specific energy of 1350 $Wh{\cdot}kg^{-1}$) [1–6].

The performance of the zinc–air battery mainly depends on the nature of the air electrode, which contains the electrocatalyst for the electrochemical reduction of oxygen. For a long time, precious metals such as platinum have been used as electrocatalysts for the electrochemical reduction of oxygen. Such catalysts endow the air electrode with high catalytic activity, strong conductivity and stability. However, the high price of the precious metals and their ability to easily contaminate are the main reasons that limit the commercial application of such catalysts [7,8]. As one of the most promising ways to replace this kind of catalyst, manganese dioxide has received long-term research and attention as a catalyst for electrochemical reduction of oxygen due to its low price and easy availability [9,10]. However, because of the slow electrochemical reduction of oxygen on the air electrode, zinc–air batteries assembled with conventional manganese dioxide as the catalyst have large polarization, which greatly limits the power density of the battery. Thus, people have carried out extensive research on electrocatalysts for ORR [11–14]. Despite all this, manganese oxide is still one of the most popular choices for ORR.

$LiMn_2O_4$ is one of the most famous electrode materials for lithium batteries until now [15,16]. Based on environmental compatibility, low cost, high electrocatalytic activity, and multiple valence states, other similar manganese-based spinel compounds have been particularly attractive as cathodic catalysts [17–23]. By contrast, LMO not only possesses lower cost, less toxicity and higher security, but it also has a stable three-dimensional

tunnel structure, which is conducive to the transfer of charges and the oxygen reduction reaction. However, there are only a few studies in the literature that are available on the electrocatalytic activity of LMO for ORR in alkaline conditions and its application in alkaline aqueous metal–air batteries. Prominent structural features of spinel $LiMn_2O_4$ urge us to conduct an examination on its catalytic activity for ORR in alkaline conditions.

2. Results and Discussion

2.1. Morphology and Structure Analysis

Morphological analysis of the as-prepared LMO is shown in Figure 1. The SEM micrograph revealed well-defined, nanoscale irregular-shaped particles. The particle sizes were in the range of 0.1 to 0.5 µm. This catalyst structure will make it possible for oxygen, catalyst powders, and the electrolyte's three-phrase interface to come into close contact with the air electrode. Furthermore, the oxygen that enters into the air electrode can be electrochemically reduced without issue.

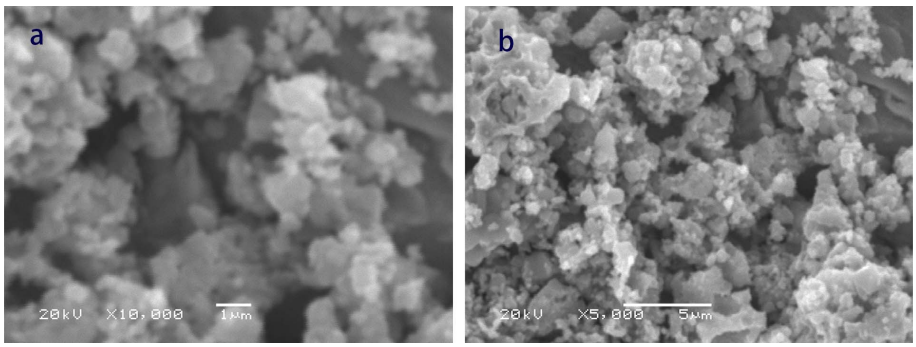

Figure 1. SEM images of the LMO at magnifications of 10,000× (**a**), 5000× (**b**).

The crystalline nature and phase characteristics of LMO were studied using XRD at a 0.02° s^{-1} scan rate in a 2θ range of 10°∼90°. Figure 2 shows the diffraction pattern of LMO. As can be seen from Figure 2a, all the diffraction peaks can be assigned to the well-known spinel phase (PDF no. 350782) with an Fd3m space group. Peaks at 2-theta 18.61°, 36.08°, 37.74°, 43.87°, 48.05°, 58.06°, 63.78°, 67.08°, 75.53°, 76.55°, 80.64°, 83.65°, correspond to the (1 1 1), (3 1 1), (2 2 2), (4 0 0), (3 3 1), (5 1 1), (4 4 0), (5 3 1), (5 3 3), (6 2 2), (4 4 4), (5 5 1), crystalline planes of LMO. The spinel structure can be described as ideally consisting of a cubic close-packing arrangement of oxygen ions at the 32e sites, the Li^+ ions occupy the tetrahedral 8a sites, and the Mn^{3+} and Mn^{4+} ions are at the octahedral 16d sites [24].

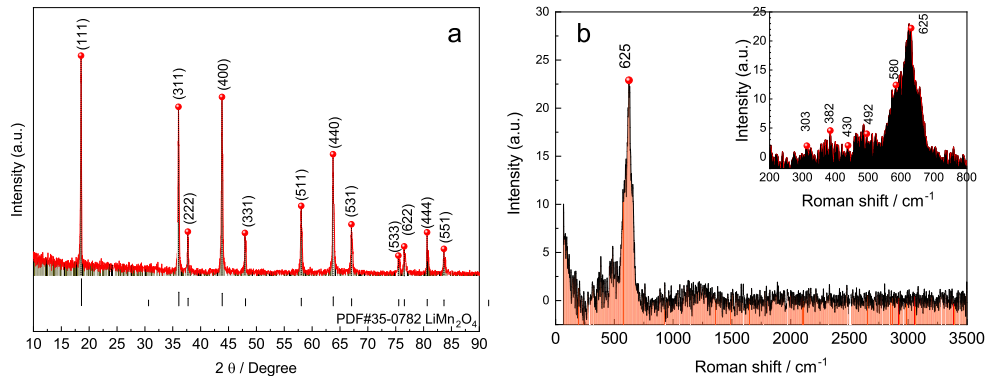

Figure 2. XRD pattern of the LMO (**a**) and Raman spectra (**b**).

In spinel oxides and in other manganese oxides, energies of ~600–650 cm^{-1} are characteristic of vibrations involving the motion of oxygen atoms inside the octahedral unit MnO_6 [25]. The assignment of modes observed in the RS spectra of the λ-$LiMn_2O_4$ spinel has been reported previously [26,27]. As shown in Figure 2b, the Raman spectra of spinel $LiMn_2O_4$ demonstrates a dominant peak at ~625 cm^{-1} in coherence with several literature reports [28,29]. The Raman band located at about 625 cm^{-1} is viewed as the symmetric Mn-O stretching vibration of MnO_6 groups. This high-wave number band is assigned to the A_{1g} species in the $O^7{}_h$ spectroscopic symmetry. Its broadness is related to the cation–anion bond lengths and polyhedral distortion occurring in $LiMn_2O_4$. As the manganese ions of the spinel structure exhibit a charge disproportionation such as $LiMn^{3+}Mn^{4+}O_4$, there are isotropic $Mn^{4+}O_6$ octahedra and locally distorted $Mn^{3+}O_6$ octahedra due to the JT effect [30]. Several smaller peaks are also detected by Raman, namely at ~580, ~492, ~430 and ~382 cm^{-1}, resembling F_{2g} symmetry. A peak located at ~303 cm^{-1} has F_{2g} symmetry of the stretching vibration of the Li-O bonds [31], but due to baseline correction, the signal is not well profound. The weak Raman scattering efficiency is attributed to the electronic properties of $LiMn_2O_4$. It is a fact that $Li[Mn^{3+}Mn^{4+}]O_4$ is a small-polaron semiconductor, in which electron hopping occurs between the two oxidation states of the manganese ions [32]. Thus, it can be stated that in the ideal cubic spinel $LiMn_2O_4$, the Mn^{3+} and Mn^{4+} cations are considered as crystallographically equivalent (16d sites) in agreement with the XRD data; $LiMn_2O_4$ has vibration modes similar to those reported by several groups [29,31].

2.2. Polarization Characteristics of the Air Electrode

Figure 3a shows the liner voltammogram (LV) recorded at an air electrode with LMO. As a comparison, the LV curve of the air electrode with EMD is also given in the figure. The cathodic currents for the air electrodes start to emerge at about −0.001 V, while the cathodic current for the electrode with LMO increases rapidly as the potential becomes more negative, whereas that of the EMD-catalyzed air electrode increases very slowly. The LMO-catalyzed-air electrode has a higher cathodic current than that of the EMD-catalyzed air electrode, indicating improved electrocatalytic activity of LMO for ORR. The difference in the polarization feature of the two electrodes should arise from the catalyst structures. Figure 3b shows the chronamperometries for the air electrodes with an LMO catalyst at different potentials. The chronoamperometry technique consists of applying a potential jump on the electrode from rest potential to a negative potential and recording the current transient. As can been seen from the figure, the cathodic currents of the air electrodes at potentials of 0.2, 0.3, and 0.4 V are all decreased sharply within 0.1 s and then achieve a nearly stable value. However, the values of the cathodic current are quite different. This result further confirms the LMO as a catalyst with good catalytic activity.

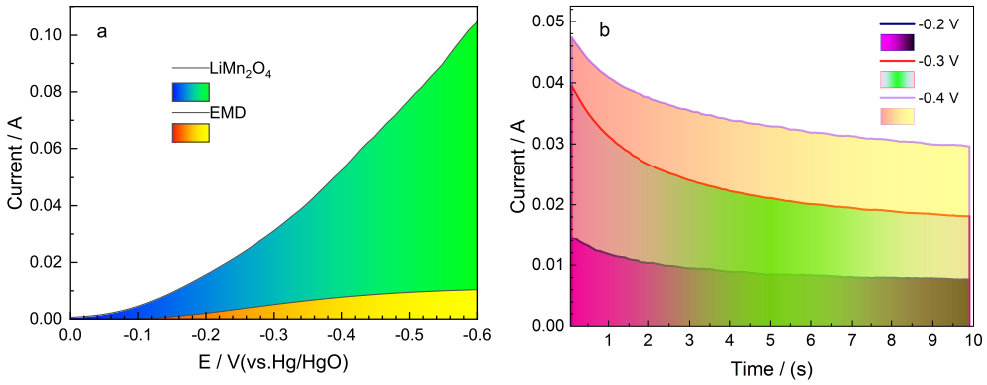

Figure 3. Linear voltammograms of air electrodes with the LMO and EMD (**a**) and chronoamperogram curves of air electrodes with the LMO (**b**).

The steady-state polarization curve test results are shown in Figure 4. As can be seen from the figure, when the current density of the oxygen electrode catalyzed by EMD is increased gradually from 0 to 80 mA·cm^{-2}, the polarization overpotential increases slowly, from −0.1 to −0.42 V. When the current density is greater than 80 mA·cm^{-2}, the overpotential value increases significantly, and the polarization overpotential value reaches −0.7 V. By contrast, the current density of the oxygen electrode catalyzed by LMO increased from 0 to 25 mA·cm^{-2}, and the overpotential increased from 0.35 to −0.20 V. Whereas when the current density was greater than 25 mA·cm^{-2}, the increasing trend of the overpotential value is quite slow, even for the current density over 80 mA·cm^{-2}, where the overpotential value reaches −0.25 V. Although the initial overpotential of the oxygen electrode catalyzed by LMO is relatively large, its value was 0.35 V; however, with the increase in current density from 25 to 100 mA·cm^{-2}, the increase in the overpotential value is almost zero. The above facts indicate that the catalytic activity and stability of the oxygen electrode catalyzed by LMO for oxygen reduction are much better than those of the EMD.

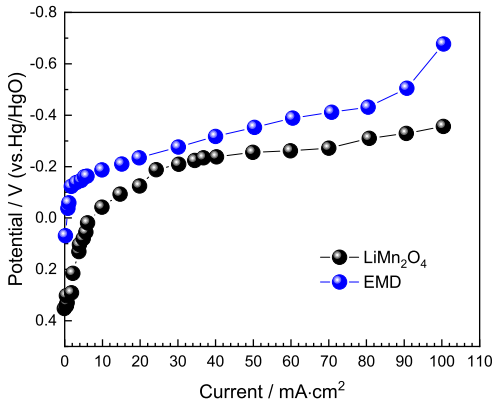

Figure 4. Polarization curves of air electrodes with LMO and EMD, respectively.

2.3. Electrochemical Impedance Spectroscopy (EIS) Study

Typical electrochemical impedance spectrum of air electrodes with the as-prepared $LiMn_2O_4$ and EMD are shown in Figure 5 in the Nyquist plot, in which the x axis and y axis represent the real part of the impedance (Z′) and the imaginary part of the impedance (Z″). From the Nyquist impedance spectra, at a high frequency region (f > 1 kHz), besides the existence of induction, the Nyquist plot is composed of a small depressed semicircle indicating the presence of reactance, which is attributed to the ohm polarization of the air electrode. At the intermediate frequency region (10 Hz < f < 1 kHz), the semicircle is caused by the electrochemical polarization of the air electrode. It also can be seen that at low frequency (f < 10 Hz), the plot tends to change to a straight line that has an angle of 45°. This straight line is a characteristic of the semi-finite diffusion (Warburg impedance Z_w). The electrolyte resistance is determined by the point of intersection of the high-frequency semicircle with the real axis [33,34].

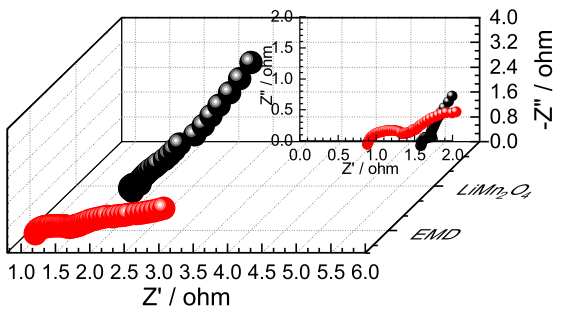

Figure 5. EIS of air electrodes with the LMO and EMD.

From the above analysis, it is evident that the difference in electrolyte resistance is 0.5 ohm for two air electrodes, whereas the interface resistance and electrochemical polarization resistance are clearly different. Specifically, the LMO-catalyzed air electrode has lower values of the interface resistance, electrochemical polarization resistance and Warburg impedance than that of the EMD-catalyzed air electrode. Thus, it can evidently be concluded that employing LMO as a catalyst is favorable to the ORR.

2.4. Electrochemical Catalytic Activity toward ORR

A rotating disk electrode (RDE) was used to study the kinetics of oxygen reduction at the LMO/Nafion-modified glassy carbon (GC) electrodes. Before recording linear sweep voltammetry (LSV) for ORR at a rate of 5 $mV{\cdot}s^{-1}$, dozens of cyclic voltammetry (CV) scans were employed to achieve stable curves. From Figure 6, the ORR currents at these two electrodes are clearly different. In the case of the EMD–catalytic electrode, there are two obvious reduction peaks located at −0.36 and −0.9 V, respectively, which means that the reaction involves two steps: the reduction of Mn^{4+} to Mn^{3+}, and oxygen reduction to OH^-. The specific reaction can be expressed as Equations (1) and (2); this experimental phenomenon is also in agreement entirely with the reported results [35,36]. In the case of the LMO catalytic electrode, the reduction current is not only large but also presents one current peak, which indicates a one-step ORR occurrence. The reaction is expressed as Equation (3) .

$$Mn^{4+} + e^- \rightarrow Mn^{3+} \quad (1)$$

$$O_2 + H_2O + 2e^- \rightarrow HO_2^- + OH^- \quad (2)$$

$$O_2 + 2H_2O + 4e^- \rightarrow 4OH^- \quad (3)$$

The ORR reaction kinetics were evaluated via the Koutechy–Levich (K-L) equation [37]:

$$\frac{1}{i} = \frac{1}{i_d} + \frac{1}{i_k} = \frac{1}{B\omega^{1/2}} + \frac{1}{i_k} \quad (4)$$

$$i_d = 0.62nFAD_0^{2/3}\omega^{1/2}\nu^{-1/6}C_o^* \quad (5)$$

$$i_k = nFAK\Gamma_{cat}C_o^* \quad (6)$$

where i, i_d, and i_k represent the measured, diffusion-limiting, and kinetic current density, respectively, and ω is the electrode's rotational rate. B can be determined from the Levich equation as follows: $B = 0.62nFAC_o{}^*D_o{}^{2/3}v^{-1/6}$, where n represents the number of electrons, F is the Faraday constant (F = 96,485 $C{\cdot}mol^{-1}$), $C_o{}^*$ is the saturated O_2 concentration (1.21×10^{-6} $mol{\cdot}cm^{-3}$), D is the diffusion coefficient of O_2 in 6.0 M KOH (1.75×10^{-5} $cm^2\ s^{-1}$), ν is the kinetic viscosity (0.01 $cm^2{\cdot}s^{-1}$) [38], K ($M^{-1}{\cdot}s^{-1}$) is the kinetic rate constant for the catalytic reaction, and Γ_{cat} ($mol{\cdot}cm^{-2}$) is the amount of catalysts on the surface of the electrode. The constant 0.62 is adopted when the rotation speed is expressed in rpm. From Equation (4), there is a line relationship between i^{-1} and $\omega^{-1/2}$, where B^{-1} and $i_k{}^{-1}$ are the slope and intercept of the line, respectively. Thus, it is necessary to extract the corresponding information from the LSV result of RDE and to make related line fittings; the Koutecky–Levich plots and fitting lines are shown in Figure 7. It can be calculated that the ORR at the LMO/Nafion-modified electrode is a four-electron process.

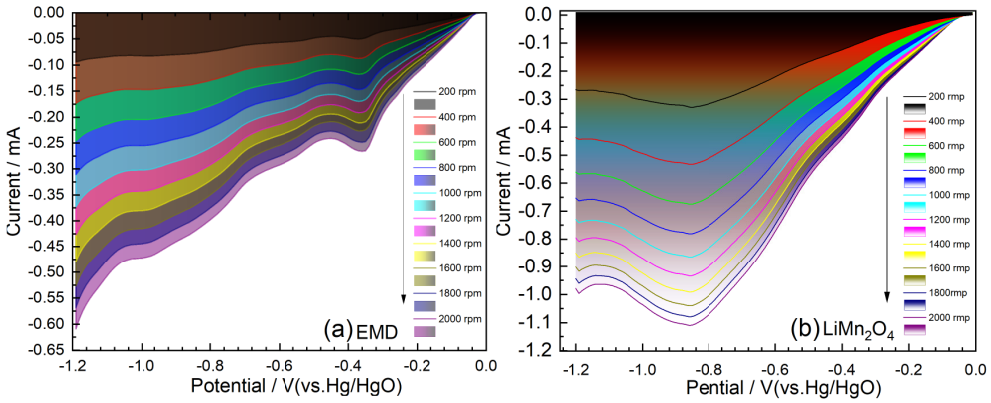

Figure 6. LSV graphs with a GC disc in the O_2-saturated 6 M KOH solution; (**a**) EMD and (**b**) LMO; scan rate of 5 mv·s^{-1}.

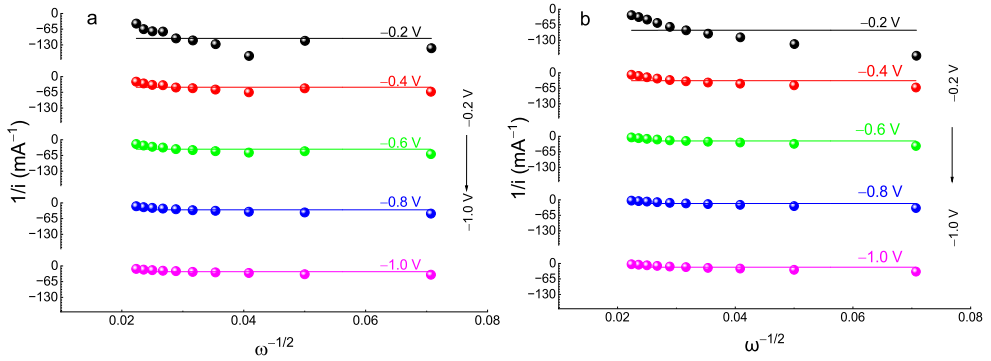

Figure 7. Koutecky–Levich plots for the EMD (**a**) and LMO (**b**) catalyst at different potentials: −0.2, −0.4, −0.6, −0.8, −1.0 V.

2.5. Discharge Characteristics of Solid-State Zinc–Air Cells

To further investigate the catalytic effectiveness of the spinel LMO, the prepared LMO was used as an air electrode catalyst to assemble a solid-state zinc–air cell, and the cell was tested under different discharge currents. At constant discharge drains of 10, 20 and 50 mA·cm^{-2} for the cells composed of 0.03 g LMO catalyst and 0.5 g zinc powder, Figure 8 shows the discharge diagram of the cell under different discharge currents. It can be seen from the figure that the discharge curve of the cell is flat, showing the characteristics of the zinc–air batteries that are different from other alkaline primary cells (such as alkaline zinc manganese primary cells, where the discharge curve is S-shaped, and the battery voltage gradually decreases with discharge time). We can see that the cells can sustain the current drain at about 0.9 V, and the flat part of the discharge curves shows its smoothness. Discharge time of the cell can last for 4.8, 1.4 and 0.3 h (5024, 2930 and 1570 mAh·g^{-1} based on the mass of catalyst, respectively). The discharge time gradually decreases with the increase in discharge current, because during the large current discharge, the internal IR drop of the cell increases, and the polarization of the cell increases, resulting in a decrease in the discharge time and a shortened discharge platform. The above discharge characteristics clearly indicate that the spinel LMO is a worth accepting as a catalyst toward solid-state zinc–air batteries.

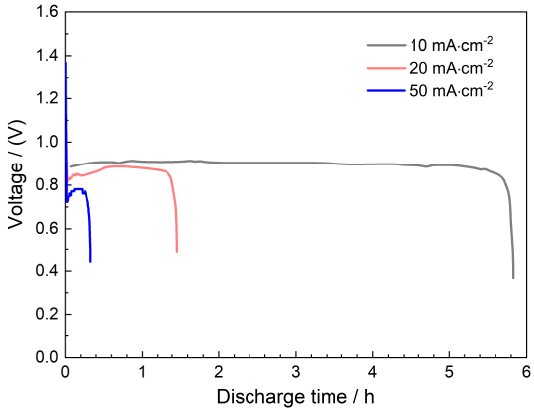

Figure 8. Discharge curves of zinc–air cells with the LMO and EMD, at 10, 20 and 50 mA·cm^{-2} current densities.

3. Materials and Methods

As per the typical synthetic process, 0.66 g of lithium hydroxide monohydrate was dissolved in 40 mL of double-distilled water. Then, 1.37 g of electrolytic manganese dioxide (EMD) was added to this solution, and the resulting slurry was held at room temperature for 0.5 h. Then, while stirring, 0.20 g of glucose was added, followed by the addition of 40 mL of water. This slurry was placed in a 100 mL Teflon-lined autoclave for hydrothermal treatment. Finally, the reaction was carried out selectively at 150 °C for 24 h. The solid product was filtered under suction and rinsed multiple times with distilled water after cooling to ambient temperature and then dried at 120 °C for at least 24 h.

To make air electrodes, a two-layer gas diffusion electrode was built, with one layer referred to as the catalyst layer or active layer and the other as the air layer or hydrophobic layer. The air layer was made up of a 2:1:7 weight ratio of active carbon, Na_2SO_4, and polytetrafluoroethylene (PTFE, from Aldrich); these chemicals were combined with ethanol to produce a dough, which was then rolled onto a porous nickel substrate. A mixture including the catalyst $LiMn_2O_4$, Na_2SO_4, and PTFE in a weight ratio of 6:2:3 was first mixed and crushed in excess ethanol; it was then rolled into a sheet with a thickness of 0.1∼0.4 m and a diameter of 20 mm, which was deposited onto the as-prepared air layer and pressed for 5 min at 3×10^7 kg·cm^{-2}. The final electrode was typically 0.2∼0.5 mm thick after drying and heat treatment at 40 °C for half hour.

Testing cells with a catalytic air electrode as the cathode, zinc powder as the anode, and an alkaline PVA gel polymer electrolyte (GPE) were built for the electrochemical studies.

Using a scanning electron microscope (SEM) (Leo-1430VP, ZEISS, Oberkochen, Germany), the morphology of the prepared $LiMn_2O_4$ was observed. Raman spectra and X-ray diffraction (XRD) were also used to examine the structure. X-ray powder diffraction (XRD) patterns were recorded at room temperature with a Siemens D 501 diffractometer, Siemens, Munich, Germany, with Cu K_α radiation. Within the range of 10° to 80°, the pattern was scanned using the step scanning mode at 0.02°(2θ) and a 1 s step^{-1} counting time. At room temperature, Raman scattering spectra were taken between 4 and 3500 cm^{-1} at room temperature by a DXR Raman microscope (DXR532, Thermo-Fisher, Waltham, MA, USA) with laser light source of 532 nm radiation.

The chronoamperometery curves and polarized profiles were recorded on the CHI 760E electrochemistry station using linear scanning voltammograms (LSV) with a scan rate of 5 mV·s^{-1} calibrated with 95% iR-compensation. Linear scanning voltammograms were recorded on a rotating disk electrode (RDE) by the CHI 760E in O_2-saturated 6 M KOH solution and the rotation rates were controlled by a 636 motor speed controller (EG&G, USA). A rotating disc electrode (RDE) with a glassy carbon (GC) electrode (6 mm diameter) was used; the electrode was pretreated as follows [39]: LMO was dispersed in 0.05 wt.% Nafion solution, and the resultant suspension was agitated in an ultrasonic bath for 10 min. After that, 20 µL of the above suspension was pipetted on the GC disc electrode

surface, which was air-dried for 30 min to evaporate the solvent, resulting in the loading of 0.56 mg·cm^{-2}; the LMO/Nafion-modified GC electrodes were thus obtained.

All measurements were performed in a three-electrode cell with the air electrode as the working electrode, Hg/HgO electrode as the reference electrode and platinum foil as the counter electrode. A 6 mol·L^{-1} KOH aqueous solution was used as the electrolyte.

The discharge characteristic of the solid-state zinc–air cell was tested with a galvanostatic charge–discharge unit (8-channel battery analyzer). All Zn–air battery tests were performed under ambient atmosphere at room temperature. Discharge power density was calculated using the data from the discharge polarized profiles using the following equation: $P = U_d \times j_d$, where P is the discharge power density, U_d is the discharge voltage, and j_d is the discharge current density.

4. Conclusions

A spinel manganese oxide $LiMn_2O_4$ was obtained successfully via a simple hydrothermal method. Physical tests including SEM, XRD and Roman spectra were conducted, and the results indicate that the as-prepared LMO possesses a typical spinel structure and nanoscale irregular-shaped morphology. Owing to a charge disproportionation of manganese ions involved in $LiMn^{3+}Mn^{4+}O_4$, the existence of the JT effect enables electron hoping between Mn^{3+} and Mn^{4+}. This special characteristic boosts the ORR from a mechanism point of view. The electrocatalytic activity experiment for ORR in alkaline condition and the discharge performance of the solid-state zinc–air cell with LMO show that the spinel LMO directly catalyzes four-electron ORR, and therefore, the solid-state zinc–air cell presents prominent discharge performance at a large current drain of 10 mA·cm^{-2}. In conclusion, spinel manganese oxides can be considered as an effective electrocatalyst toward ORR in alkaline condition; at the same time, the exploratory attempt of spinel manganese oxide toward ORR provides a new reference for the further development and application of manganese oxide-based catalysts toward ORR and relative batteries.

Author Contributions: Conceptualization, G.Z. and B.J.; methodology, G.Z.; software, G.Z.; validation, P.Z.; formal analysis, S.K.; investigation, S.K.; data curation, S.K.; writing—original draft preparation, G.Z.; writing—review and editing, G.Z.; visualization, S.K.; supervision, G.Z.; project administration, G.Z.; funding acquisition, G.Z. All authors have read and agreed to the published version of the manuscript.

Funding: This research was funded by National Foundation of Science of China, grant number 21443004, by the 47th (1792) Scientific Research Foundation for the Returned Overseas Chinese Scholars, and by the Chunhui Program of Ministry of Education of China (Z2014083, Z2014084).

Data Availability Statement: The data presented in this study are available within the article. We are working to make the codes underlying this study available on Github.

Conflicts of Interest: The authors declare no conflict of interest.

References

1. Xin, F.; Zhou, H.; Chen, X.; Zuba, M.; Chernova, N.; Zhou, G.; Whittingham, M.S. Li–Nb–O Coating/Substitution Enhances the Electrochemical Performance of the $LiNi_{0.8}Mn_{0.1}Co_{0.1}O_2$ (NMC 811) Cathode. *ACS Appl. Mater. Interfaces* **2019**, *11*, 34889–34894. [CrossRef] [PubMed]
2. Dou, H.; Xu, M.; Zheng, Y.; Li, Z.; Wen, G.; Zhang, Z.; Yang, L.; Ma, Q.; Yu, A.; Luo, D.; et al. Bioinspired Tough Solid-State Electrolyte for Flexible Ultralong-Life Zinc-Air Battery. *Adv. Mater.* **2022**, *34*, 2110585. [CrossRef] [PubMed]
3. Wang, S.; Xu, J.; Wang, W.; Wang, G.J.N.; Rastak, R.; Molina-Lopez, F.; Chung, J.W.; Niu, S.; Feig, V.R.; Lopez, J.; et al. Skin Electronics from Scalable Fabrication of an Intrinsically Stretchable Transistor Array. *Nature* **2018**, *555*, 83–88. [CrossRef] [PubMed]
4. Zhao, S.; Xia, D.; Li, M.; Cheng, D.; Wang, K.; Meng, Y.S.; Chen, Z.; Bae, J. Self-Healing and Anti-CO_2 Hydrogels for Flexible Solid-State Zinc-Air Batteries. *ACS Appl. Mater. Interfaces* **2021**, *13*, 12033–12041. [CrossRef]
5. Zhu, J.; Xiao, M.; Zhang, Y.; Jin, Z.; Peng, Z.; Liu, C.; Chen, S.; Ge, J.; Xing, W. Metal–Organic Framework-Induced Synthesis of Ultrasmall Encased NiFe Nanoparticles Coupling with Graphene as an Efficient Oxygen Electrode for a Rechargeable Zn–Air Battery. *ACS Catal.* **2016**, *6*, 6335–6342. [CrossRef]
6. Zhu, X.; Hu, C.; Amal, R.; Dai, L.; Lu, X. Heteroatom-doped Carbon Catalysts for Zinc–air Batteries: Progress, Mechanism, and Opportunities. *Energy Environ. Sci.* **2020**, *13*, 4536–4563. [CrossRef]

7. Tiwari, J.N.; Nath, K.; Kumar, S.; Tiwari, R.N.; Kemp, K.C.; Le, N.H.; Youn, D.H.; Lee, J.S.; Kim, K.S. Stable Platinum Nanoclusters on Genomic DNA–graphene Oxide with a High Oxygen Reduction Reaction Activity. *Nat. Commun.* **2013**, *4*, 2221. [CrossRef]
8. Nesselberger, M.; Roefzaad, M.; Fayçal Hamou, R.; Ulrich Biedermann, P.; Schweinberger, F.F.; Kunz, S.; Schloegl, K.; Wiberg, G.K.H.; Ashton, S.; Heiz, U.; et al. The Effect of Particle Proximity on the Oxygen Reduction Rate of Size-selected Platinum Clusters. *Nat. Mater.* **2013**, *12*, 919–924. [CrossRef]
9. Chung, T.D.; Anson, F.C. Catalysis of the Electroreduction of O_2 by Cobalt 5,10,15,20-tetraphenylporphyrin Dissolved in Thin Layers of Benzonitrile on Graphite Electrodes. *J. Electroanal. Chem.* **2001**, *508*, 115–122. [CrossRef]
10. Zeng, K.; Zheng, X.; Li, C.; Yan, J.; Tian, J.; Jin, C.; Strasser, P.; Yang, R. Recent Advances in Non-Noble Bifunctional Oxygen Electrocatalysts toward Large-Scale Production. *Adv. Funct. Mater.* **2020**, *30*, 2000503. [CrossRef]
11. Watanabe, M.; Tryk, D.A.; Wakisaka, M.; Yano, H.; Uchida, H. Overview of Recent Developments in Oxygen Reduction Electrocatalysis. *Electrochim. Acta* **2012**, *84*, 187–201. [CrossRef]
12. Yang, D.; Zhang, L.; Yan, X.; Yao, X. Recent Progress in Oxygen Electrocatalysts for Zinc-Air Batteries. *Small Methods* **2017**, *1*, 1700209. [CrossRef]
13. Zhu, C.; Li, H.; Fu, S.; Du, D.; Lin, Y. Highly Efficient Nonprecious Metal Catalysts towards Oxygen Reduction Reaction Based on Three-dimensional Porous Carbon Nanostructures. *Chem. Soc. Rev.* **2016**, *45*, 517–531. [CrossRef] [PubMed]
14. Li, Y.; Gong, M.; Liang, Y.; Feng, J.; Kim, J.E.; Wang, H.; Hong, G.; Zhang, B.; Dai, H. Advanced Zinc-air Batteries Based on High-performance Hybrid Electrocatalysts. *Nat. Commun.* **2013**, *4*, 1805. [CrossRef]
15. Joo, H.; Lee, J.; Yoon, J. Short Review: Timeline of the Electrochemical Lithium Recovery System Using the Spinel $LiMn_2O_4$ as a Positive Electrode. *Energies* **2020**, *13*, 6235. [CrossRef]
16. Iskandar Radzi, Z.; Helmy Arifin, K.; Zieauddin Kufian, M.; Balakrishnan, V.; Rohani Sheikh Raihan, S.; Abd Rahim, N.; Subramaniam, R. Review of Spinel $LiMn_2O_4$ Cathode Materials under High Cut-off Voltage in Lithium-ion Batteries: Challenges and Strategies. *J. Electroanal. Chem.* **2022**, *920*, 116623. [CrossRef]
17. Liu, Y.; Li, J.; Li, W.; Li, Y.; Chen, Q.; Liu, Y. Spinel $LiMn_2O_4$ nanoparticles dispersed on nitrogen-doped reduced graphene oxide nanosheets as an efficient electrocatalyst for aluminium-air battery. *Int. J. Hydrog. Energy* **2015**, *40*, 9225–9234. [CrossRef]
18. Leng, L.; Li, J.; Zeng, X.; Song, H.; Shu, T.; Wang, H.; Ren, J.; Liao, S. Spinel $LiMn_2O_4$ Nanoparticles Grown in Situ on Nitrogen-Doped Reduced Graphene Oxide as an Efficient Cathode for a Li-O_2/Li-Ion Twin Battery. *ACS Sustain. Chem. Eng.* **2018**, *7*, 430–439. [CrossRef]
19. Yang, H.B.; Miao, J.; Hung, S.F.; Chen, J.; Tao, H.B.; Wang, X.; Zhang, L.; Chen, R.; Gao, J.; Chen, H.M.; et al. Identification of catalytic sites for oxygen reduction and oxygen evolution in N-doped graphene materials: Development of highly efficient metal-free bifunctional electrocatalyst. *Sci. Adv.* **2016**, *2*, e1501122. [CrossRef]
20. Zhai, X.; Yang, W.; Li, M.; Lv, G.; Liu, J.; Zhang, X. Noncovalent hybrid of $CoMn_2O_4$ spinel nanocrystals and poly (diallyldimethylammonium chloride) functionalized carbon nanotubes as efficient electrocatalysts for oxygen reduction reaction. *Carbon* **2013**, *65*, 277–286. [CrossRef]
21. Wang, D.; Chen, X.; Evans, D.G.; Yang, W. Well-dispersed Co_3O_4/Co_2MnO_4 nanocomposites as a synergistic bifunctional catalyst for oxygen reduction and oxygen evolution reactions. *Nanoscale* **2013**, *5*, 5312. [CrossRef] [PubMed]
22. Wu, Q.; Jiang, L.; Qi, L.; Wang, E.; Sun, G. Electrocatalytic performance of Ni modified MnO_x/C composites toward oxygen reduction reaction and their application in Zn-air battery. *Int. J. Hydrog. Energy* **2014**, *39*, 3423–3432. [CrossRef]
23. Liu, J.; Jiang, L.; Zhang, B.; Jin, J.; Su, D.S.; Wang, S.; Sun, G. Controllable Synthesis of Cobalt Monoxide Nanoparticles and the Size-Dependent Activity for Oxygen Reduction Reaction. *ACS Catal.* **2014**, *4*, 2998–3001. [CrossRef]
24. Mandal, S.; Rojas, R.M.; Amarilla, J.M.; Calle, P.; Kosova, N.V.; Anufrienko, V.F.; Rojo, J.M. High Temperature Co-doped $LiMn_2O_4$-Based Spinels. Structural, Electrical, and Electrochemical Characterization. *Chem. Mater.* **2002**, *14*, 1598–1605. [CrossRef]
25. Julien, C.; Massot, M.; Rangan, S.; Lemal, M.; Guyomard, D. Study of Structural Defects in γ-MnO_2 by Raman Spectroscopy. *J. Raman Spectrosc.* **2002**, *33*, 223–228. [CrossRef]
26. Sinha, M.; Gupta, H. Study of Zone-center Phonons in Lithium Manganese Oxide. *Phys. B Condens. Matter* **2002**, *316–317*, 166–169. [CrossRef]
27. Ammundsen, B.; Burns, G.R.; Islam, M.S.; Kanoh, H.; Rozière, J. Lattice Dynamics and Vibrational Spectra of Lithium Manganese Oxides: A Computer Simulation and Spectroscopic Study. *J. Phys. Chem. B* **1999**, *103*, 5175–5180. [CrossRef]
28. Julien, C. Techniques for the Characterization of New Cathode Materials. In *Trends in Materials Science*; Narosa: New Delhi, India, 1997; pp. 44–63.
29. Ramana, C.V.; Massot, M.; Julien, C.M. XPS and Raman Spectroscopic Characterization of $LiMn_2O_4$ Spinels. *Surf. Interface Anal.* **2005**, *37*, 412–416. [CrossRef]
30. Julien, C.M.; Massot, M. Raman Spectroscopic Studies of Lithium Manganates with Spinel Structure. *J. Phys. Condens. Matter* **2003**, *15*, 3151–3162. [CrossRef]
31. Lu, J.; Zhan, C.; Wu, T.; Wen, J.; Lei, Y.; Kropf, A.J.; Wu, H.; Miller, D.J.; Elam, J.W.; Sun, Y.K.; et al. Effectively Suppressing Dissolution of Manganese from Spinel Lithium Manganate via a Nanoscale Surface-doping Approach. *Nat. Commun.* **2014**, *5*, 5693. [CrossRef]
32. Goodenough, J.; Manthiram, A.; Wnetrzewski, B. Electrodes for Lithium Batteries. *J. Power Sources* **1993**, *43*, 269–275. [CrossRef]

33. Hu, J.; Shi, Z.; Wang, X.; Qiao, H.; Huang, H. Silver-modified Porous 3D Nitrogen-doped Graphene Aerogel: Highly Efficient Oxygen Reduction Electrocatalyst for Zn-Air Battery. *Electrochim. Acta* **2019**, *302*, 216–224. [CrossRef]
34. Rao, C.S.; Gunasekaran, G. Cobalt-Lead-Manganese Oxides Combined Cathode Catalyst for Air Electrode in Zinc-air Battery. *Electrochim. Acta* **2015**, *176*, 649–656. [CrossRef]
35. Linden, D.; Reddy, T. *Handbook of Batteries*; McGraw Hill Professional: New York, NY, USA, 2001.
36. Cao, Y.; Yang, H.; Ai, X.; Xiao, L. The Mechanism of Oxygen Reduction on MnO_2-catalyzed Air Cathode in Alkaline Solution. *J. Electroanal. Chem.* **2003**, *557*, 127–134. [CrossRef]
37. Jiang, R.; Chu, D. Multiple Small Potential Steps at a Rotating Disk Electrode and Applications. *Electrochim. Acta* **2000**, *45*, 4025–4030. [CrossRef]
38. Jiang, R.; Anson, F.C. The Origin of Inclined Plateau Currents in Steady-state Voltammograms for Electrode Processes Involving Electrocatalysis. *J. Electroanal. Chem. Interfacial Electrochem.* **1991**, *305*, 171–184. [CrossRef]
39. Ohsaka, T.; Mao, L.; Arihara, K.; Sotomura, T. Bifunctional Catalytic Activity of Manganese Oxide toward O_2 Reduction: Novel Insight into the Mechanism of Alkaline Air Electrode. *Electrochem. Commun.* **2004**, *6*, 273–277. [CrossRef]